

# Embedded Fracture Model for Coupled Flow and Geomechanics

I. Shovkun and T. Garipov and H. A. Tchelepi

Energy Resources Engineering, Stanford University, USA

**Abstract:** Fluid injection and production cause changes in reservoir pressure, which result in deformations in the subsurface. This phenomenon is particularly important in reservoirs with abundant fractures and faults because the induced slip and opening of the fractures may significantly alter their hydraulic properties. Modeling strongly coupled poro-mechanical processes in naturally fractured reservoirs is a challenging problem. The Discrete Fracture Model (DFM) is a state-of-art method for modeling coupled flow and mechanics in fractured reservoirs. This method requires constructing computational grids that conform to fractures, which is very challenging in complex 3D settings. The objective of this study is to develop a numerical method that does not require gridding near fractures and can efficiently model hydromechanical interactions in fractured reservoirs. We utilize formulations based on the Strong Discontinuity Approach (SDA) for mechanics and Embedded Discrete Fracture Model (EDFM) for flow. We first present a mathematical formulation and emphasize the kinematic aspects of fracture slip and opening. We then introduce a series of mechanical tests that investigate the spatial convergence of the model and compare its accuracy with the Discrete Fracture Model (DFM). We finally consider a synthetic coupled case of a reservoir with several fractures and compare the performance of the SDA and DFM methods. Our results indicate super-linear spatial convergence of the proposed SDA algorithm. Numerical simulations confirm the applicability of the proposed method to modeling the coupling effects in subsurface applications.

*Keywords:* Embedded Discrete Fracture Model, Strong Discontinuity Approach, Geomechanics, Reservoir Simulation.

# 1 Introduction

Field operations in petroleum, geothermal, and waste disposal applications frequently involve injecting and withdrawing fluids from the subsurface. Changes in reservoir pressure in naturally fractured reservoirs can lead to reactivation of natural fractures and faults [Grasso, 1992, Zoback and Zinke, 2002, Rutledge et al., 2004, Zoback and Gorelick, 2012, Hwang et al., 2015]. Fault reactivation often leads to shear of the wellbore casing or damage of the reservoir integrity [Elf-Aquitaine, 1992, Wiprut and Zoback, 2000]. In tight rocks, fracture reactivation may cause significant changes in reservoir permeability [Min et al., 2004].

Modeling fracture reactivation is possible with a variety of numerical methods. It has been shown that the Finite Element Method (FEM) with discrete fracture representation (DFM) is an accurate and efficient method for modeling discontinuities in porous media [Cappa and Rutqvist, 2011, Fu et al., 2016, Salimzadeh et al., 2018]. This method, however, requires the usage of sophisticated gridding techniques for preparing high-quality computational grids. The Extended/Generalized Finite Element (xFEM) and Phase-Field methods allow to handle arbitrary fracture geometries and, therefore, suit for modeling fracture propagation [Duarte et al., 2000, Heister et al., 2015]. These methods introduce additional global variables to improve the representation of the deformation field [Haddad and Sepehrnoori, 2015, Shovkun and Espinoza, 2018]. This leads to a significant computational overhead compared to conventional FE-based methods. Several approaches to modeling fractures have been developed based on non-local formulations of continuum mechanics. Peridynamics and Discrete Element methods are among the most capable techniques for modeling complex geometrical fracture configurations [Zhao et al., 2009, Ouchi et al., 2015, Sun et al., 2016]. Similarly to xFEM and Phase-Field, however, these non-local methods have very high computational cost. The Boundary Element and Displacement Discontinuity methods are very efficient techniques; they are widely applied to mechanical problems with fractures [Olson, 2008, Sesetty et al., 2012]. These methods allow to model reservoirs with high numbers of fractures; however, they cannot capture heterogeneous and anisotropic rock properties [McClure, 2012]. It has been shown that the Boundary Element methods can be combined with the Finite Element methods to solve coupled hydro-mechanical problems [Norbeck et al., 2016].

Another type of Finite Element mechanical models is based on the Strong Discontinuity Approach (SDA) [Oliver, 1996]. This method uses the “embedded” fracture representation and can be applied to model fracture activation and propagation [Oliver et al., 1999]. The method shares similarities with xFEM but captures the deformation of discontinuity locally [Linder and Armero, 2007]. The nonlinear return mapping

algorithm allows SDA to reduce the number of degrees of freedom to that of a linear elastic system without fractures [Regueiro and Borja, 2001]. This localization allows seamless incorporation of the method into the existing Finite Element software and renders the method very attractive from the numerical simulation standpoint [Mosler, 2005].

There are several numerical techniques to simulate fluid flow in fractured formations. Dual permeability and dual porosity models [Warren et al., 1963], the Discrete Fracture Network approach (DFN) [Cacas et al., 1990], Discrete Fracture Models [Karimi-Fard et al., 2004], and the Multiple Interacting Continua (MINC) [Narasimhan and Pruess, 1988, Pruess, 1992] methods are widely used in the industry. Several approaches based on local permeability modification have been proposed to model flow in fracture media in an upscaled dual-porosity fashion [Gong et al., 2008, Li et al., 2015]. The application of the Finite Volume method with the embedded fracture representation (EDFM) has been investigated for the past decade [Li et al., 2008, ?].

While substantial research exists on using SDA in solid mechanics, very few studies investigate the application of SDA to coupled flow-mechanical problems. The approach of enriching a global variable to approximate a discontinuity used in SDA was also applied to model discontinuities in fluid pressure [Alfaiate et al., 2010]. The authors, however, did not consider hydraulically active fractures with flow within them. A combination of SDA enrichments for both displacement and flow discontinuities can be used to model the coupled behavior of fractured media [Callari and Armero, 2002]. This approach and the aforementioned SDA model for flow [Alfaiate et al., 2010] do not allow to model highly conductive fractures.

A recent advancement combined a mechanical model with embedded fracture representation and a conventional EDFM for flow [Deb and Jenny, 2017]. In their work, Deb and Jenny utilized the Extended Finite Volume method with a stabilization term for fracture activation. Their model, however, is limited to a 2D setting and slipping fractures, and it treats the fracture jump as an independent variable. An approach that consists of a Finite Element mechanical model with SDA and an embedded fracture model for flow would allow to model reservoirs with conductive fractures efficiently.

In this manuscript, we present a new hybrid numerical method for modeling coupled fluid flow and geomechanics with embedded fracture representation. We combine an FEM-based mechanical SDA model and an FVM-based flow EDFM model, which, to the best of our knowledge, has not been done before. The mechanical formulation utilizes SDA with the return-mapping algorithm [Borja, 2013]. This paper consists of comparison cases between the proposed EDFM model and the DFM model described in [Garipov et al.,

2016]. We first investigate the spatial convergence of the mechanical SDA model in plane strain scenarios with single fractures. Second, we investigate the spatial convergence of the EDFM flow model on a single-phase stationary problem. We finally compare the results produced by the EDFM and DFM models in a coupled 3D case with several fractures.

## 2 Theory

In this section, we introduce a system of equations that describes coupled fluid flow and rock deformations in a saturated porous medium with fractures. We employ linear poroelasticity equations and Darcy's law to describe the single-phase flow and mechanics within a compressible porous medium [Coussy, 2004]. We then outline the governing equations for single-phase flow within fractures and corresponding fractures deformations.

### 2.1 Porous media

#### 2.1.1 Fluid flow

The mass conservation of a single-phase fluid in a porous medium follows the continuity equation

$$\frac{\partial(\rho_f \phi)}{\partial t} = \nabla \cdot (\rho_f \mathbf{v}) + Q_{FM}, \quad (1)$$

where  $\rho_f$  is the fluid density,  $\phi$  is the rock porosity,  $\mathbf{v}$  is the fluid superficial velocity,  $Q_{FM}$  is the mass flux from the fracture into the matrix, and  $t$  is the time. Assuming that in an isothermal system a slightly compressible fluid

$$\frac{d\rho_f}{dp_M} = c_f \rho_f, \quad (2)$$

complies with the Darcy's law

$$\mathbf{v} = -\frac{\mathbf{k}_M}{\mu_f} (\nabla p_M - \rho_f \mathbf{g}) \quad (3)$$

and that the poroelastic solid is linear and isotropic

$$d\phi = b d(\nabla \cdot \mathbf{u}) + \frac{1}{K} (1 - b) (b - \phi) dp_M, \quad (4)$$

Eq. (1) becomes [Coussy, 2010]:

$$\frac{1}{M} \frac{\partial p_M}{\partial t} + b \frac{\partial (\nabla \cdot \mathbf{u})}{\partial t} - \nabla \cdot \frac{\mathbf{k}_M}{\mu_f} (\nabla p_M - \rho_f \mathbf{g}) = q_{MF}, \quad (5)$$

where  $\mathbf{u}$  is the solid matrix displacement,  $b$  is the rock Biot coefficient,  $\mathbf{k}_M$  is the matrix permeability,  $\mu_f$  is the fluid viscosity,  $\rho_f$  is the fluid mass density,  $M = \phi c_f + 1/K(1-b)(b-\phi)$  is the Biot modulus,  $K$  is the drained bulk modulus of the rock,  $\mathbf{g}$  is the gravity acceleration constant, and  $q_{MF} = Q_{MF}/\rho_F$  is the volumetric matrix-fracture flux.

### 2.1.2 Mechanical equilibrium

The mechanical equilibrium of the system is described by the quasi-static Cauchy equation:

$$\nabla \cdot \mathbf{S} = -\rho_b \mathbf{g} \quad (6)$$

where  $\mathbf{S}$  is the total stress tensor and  $\rho_b$  is the bulk mass density of the saturated rock. We use the following isotropic relation between total and effective stresses [Zoback, 2013]:

$$\mathbf{S} = \boldsymbol{\sigma} + b p_M \mathbf{I} \quad (7)$$

where  $\boldsymbol{\sigma}$  is the effective stress tensor,  $p$  is pore pressure,  $b$  is the scalar Biot coefficient, and  $\mathbf{I}$  is the second-order unit tensor. We further assume a linear relationship between the stress and strain tensors:

$$\boldsymbol{\sigma} = \mathbf{C} : \boldsymbol{\varepsilon}, \quad (8)$$

where  $\mathbf{C}$  is the fourth-order linear elastic stiffness tensor.

## 2.2 Fractures

### 2.2.1 Fluid flow

The governing equation of the fluid flow in fractures is very similar to that in the matrix. We neglect, however, the coupling terms that describe the changes in matrix aperture permeability due to pressure perturbations:

$$c_f \frac{\partial p_F}{\partial t} - \nabla \cdot \frac{\mathbf{k}_F}{\mu_f} (\nabla p_F - \rho_f \mathbf{g}) = q_{FF} - q_{MF} \quad (9)$$

where  $c_f$  is the fluid compressibility,  $p_F$  is the fluid pressure in the fracture,  $F$  is the fracture permeability,  $q_{FF}$  is the flux between intersecting fractures. The computation of the terms  $q_{FF}$  and  $q_{MF}$  is discussed in Section 3.1.

### 2.2.2 Contact mechanics

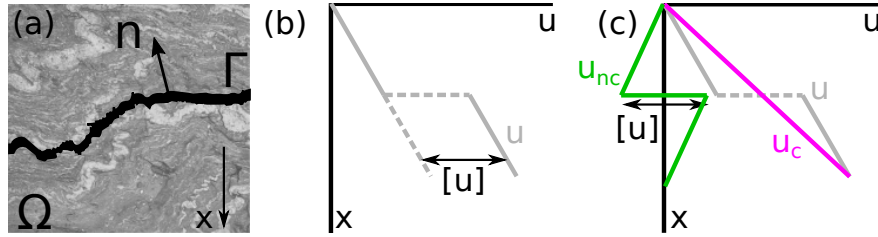


Figure 1: (a) A body  $\Omega$  that contains a discontinuity  $\Gamma$  with a normal  $\mathbf{n}$ . (b) Displacement field exhibits a jump across the fracture. (c) Decomposition of the displacement field into a conforming (regular) and non-conforming (singular) parts.

**Kinematics:** We further consider a domain  $\Omega$  separated by a two-dimensional surface  $\Gamma$  that represents a fracture (Fig. 1a). Since fractures are discontinuities, the displacement field  $\mathbf{u}$  is discontinuous (Fig. 1b) and can be decomposed as [Simo and Oliver, 1994]

$$\mathbf{u} = \bar{\mathbf{u}} + [\mathbf{u}] H_{\Gamma}, \quad (10)$$

where  $[\mathbf{u}]$  is the jump vector and  $H_{\Gamma}$  is the Heaviside step function that is equal to zero on one side of  $\Gamma$  and equal to one on the other side. SDA modifies Eq. 10 by adding and subtracting a continuous scalar function  $f$

$$\mathbf{u} = \underbrace{\bar{\mathbf{u}} + [\mathbf{u}] f}_{\mathbf{u}_c} + \underbrace{[\mathbf{u}] (H_{\Gamma} - f)}_{\mathbf{u}_{nc}} \quad (11)$$

so that  $\mathbf{u}_c$  is the conformal part of displacement,  $\mathbf{u}_{nc}$  is the non-conformal part of displacement [Simo and Oliver, 1994] as shown in Fig. 1c. The form of the level-set (or ramp) function  $f$  depends on the discretization and is discussed elsewhere [Oliver et al., 2003, Foster et al., 2007]. An expression for the small strain  $\boldsymbol{\varepsilon}$  can be obtained by taking a symmetric gradient of Eq 11:

$$\boldsymbol{\varepsilon} = \nabla^s \mathbf{u} = \nabla^s \mathbf{u}_c - ([\mathbf{u}] \otimes \nabla f)^s + (H_{\Gamma} - f) \nabla^s [\mathbf{u}] + ([\mathbf{u}] \otimes \mathbf{n})^s \delta_{\Gamma} \quad (12)$$

where  $\delta_\Gamma$  is the Dirac delta-function and  $\mathbf{n}$  is the unit normal vector to the fracture surface. We neglect the second term in the right-hand side of Eq. 12 due to the jump-discontinuity assumption, so that Eq. 12 becomes [Mosler, 2005]

$$\boldsymbol{\varepsilon} = \nabla^s \mathbf{u}_c - ([\mathbf{u}] \otimes \nabla f)^s + ([\mathbf{u}] \otimes \mathbf{n})^s \delta_\Gamma \quad (13)$$

**Plasticity formulation for SDA:** We incorporate SDA into the non-associated plasticity framework described by the system [Oliver, 1996, Mosler, 2005, Foster et al., 2007]:

$$\dot{\boldsymbol{\sigma}} = \mathbf{C} : (\dot{\boldsymbol{\varepsilon}} - \dot{\boldsymbol{\varepsilon}}^p) \quad (14a)$$

$$\dot{\boldsymbol{\varepsilon}}^p = \lambda \frac{\partial G}{\partial \boldsymbol{\sigma}} \quad (14b)$$

$$\dot{q} = \lambda H \frac{\partial G}{\partial q} \quad (14c)$$

$$F(\boldsymbol{\sigma}, q) = 0 \quad (14d)$$

where  $\boldsymbol{\varepsilon}^p$  is the plastic strain,  $\lambda$  is the plastic multiplier,  $q$  is the stress-like internal variable,  $G$  and  $F$  are the plastic potential and yield function, respectively, and  $H$  is the softening/hardening parameter. In system (14), Eq. 14a is the stress-strain relation. Eq. 14b described the plastic strain evolution. Eq. 14c is the softening/hardening law, and Eq. 14d is the yield surface. We emphasize that the system (14) contains the effective stress  $\boldsymbol{\sigma}$  as opposed to the total stress  $\mathbf{S}$  [Callari et al., 2010].

The governing system of equation for SDA can be obtained by substituting Eq. 13 into system (14), assuming that the stress  $\boldsymbol{\sigma}$  is bounded and that the distributions of the plastic multiplier  $\lambda = \lambda_\delta \delta_\Gamma$  and hardening modulus  $H = H_\Gamma \delta_\Gamma$  are singular [Simo et al., 1993, Mosler and Meschke, 2003]:

$$\dot{\boldsymbol{\sigma}} = \mathbf{C} : [\nabla^s \dot{\mathbf{u}}_c - ([\dot{\mathbf{u}}] \otimes \nabla f)^s] \quad (15a)$$

$$[\dot{\mathbf{u}}] = \lambda_\delta \frac{\partial G}{\partial \boldsymbol{\sigma}} \quad (15b)$$

$$\dot{q} = -\lambda_\delta H_\delta \frac{\partial G}{\partial q} \quad (15c)$$

$$F(\boldsymbol{\sigma}, q) = 0 \quad (15d)$$

### 2.2.3 Forms of plastic potential

In this section, we specify the flow rule and plastic potential for three possible states of a fracture: slip, opening, and stick.

**Slip:** During slip, the jump vector in the fracture is nearly-parallel to its surface. We use the following flow rule and plastic potential to impose friction in the fracture:

$$F(\mathbf{t}, q) = t_\tau - \mu t_n - q \quad (16a)$$

$$G(\mathbf{t}, q) = t_\tau - \theta t_n - q \quad (16b)$$

where  $t_\tau = \mathbf{n} \cdot \boldsymbol{\sigma} \cdot \boldsymbol{\tau}$  is the tangent traction,  $t_n = \mathbf{n} \cdot \boldsymbol{\sigma} \cdot \mathbf{n}$  is the normal traction,  $\mu$  is the tangent of the friction angle, and  $\theta$  is the tangent of the dilation angle. Eq. 16b transforms Eq. 15b into

$$[\dot{u}]_n = \theta \lambda \quad (17)$$

$$[\dot{u}]_\tau = \lambda$$

where  $[\dot{u}]_n$  and  $[\dot{u}]_\tau$  are the normal and tangential components of  $[\dot{u}]$ .

**Opening:** For an open fracture, we propose to use three components of the jump function  $[u]$  as independent local variables. We select the flow rule and plastic potential to enforce the absence of all traction components independently:

$$F_1(\mathbf{t}, q) = G_1(\mathbf{t}, q) = t_n - q$$

$$F_2(\mathbf{t}, q) = G_2(\mathbf{t}, q) = t_{\tau_1} - q \quad (18)$$

$$F_3(\mathbf{t}, q) = G_3(\mathbf{t}, q) = t_{\tau_2} - q$$

Note that in the case of an opening fracture the plastic potential  $G$  and flow rule  $F$  are equal (associative plasticity) and have three components. This choice of the plastic potential transforms Eq. 15b to the following form:

$$[\dot{u}]_{\tau_1} = \lambda_1$$

$$[\dot{u}]_{\tau_2} = \lambda_2 \quad (19)$$

$$[\dot{u}]_n = \lambda_3$$

**Stick:** The case of a closed non-slipping fracture (stick case) also requires special treatment. Although during loading, a rock with a fracture behaves elastically until the yield conditions are met, it is important to enforce the zero-normal jump and no-slip conditions during the unloading of a fracture:

$$[u]_n = 0 \quad (20)$$

$$[\dot{u}]_\tau = 0$$

We emphasize that we set the normal jump and tangential jump rate to zero.



### 3 Discretization

Our numerical model for embedded fractures utilizes a hybrid formulation with first-order Galerkin displacement approximation, Petrov-Galerkin for the enhanced strain approximations, and piecewise-constant finite-volume representation of pressure. The distribution of variables in a cell is shown in Fig. 3. Due to the choice of shape functions, the conforming displacement is defined at grid nodes. As discussed in Section 2.2.2, the displacement jump  $[\mathbf{u}]$  on the fracture is assumed to be discontinuous and is approximated as a piecewise-constant function. We define the displacement jump at the cell centers, although, as discussed in Section 3.2, its location is irrelevant. Fluid pressure in the rock matrix and fracture is defined in the matrix and fracture control volume centers, respectively.

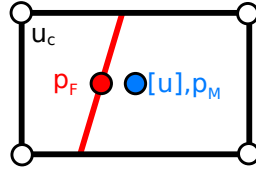


Figure 2: Location of variables in the coupled formulation. The conforming displacement  $u_c$  is defined in cell vertices. The jump  $[\mathbf{u}]$  and the fluid pressure in the rock matrix  $p_M$  are defined at the cell centers. The fluid pressure  $p_M$  in the fracture is defined at the center of the fracture control volume.

In the following sections, we provide the relevant details regarding the numerical treatment of fractures. We first discuss fluid flow and then provide the details of discretizing the mechanics equilibrium equations.

#### 3.1 Fluid flow in fractures

The EDFM approach for approximating fluid flow consists of approximating the matrix-fracture flow  $q_{MF}$  and fracture-fracture flow  $q_{FF}$  terms in Eq. 5 and 9. We opt to select a simplified approach first introduced in [Li et al., 2008]. More accurate schemes are available as discussed in Section 5.3.

We compute the total mass flux between a reservoir control volume and a fracture control volume as:

$$Q_{MF} = \frac{2A \mathbf{n} \cdot \mathbf{k}_R \cdot \mathbf{n} \rho_f}{\bar{d} \mu_f} (p_M - p_F), \quad (21)$$

where the coefficient  $\bar{d}$  is the average distance between the points in the reservoir cell and the fracture cells. When a fracture element with its center in  $\mathbf{M}_F$  bisects a cell with the volume  $V_0$  and the center in  $\mathbf{M}_0$ , then

the initial volume splits into shape I with the center in  $\mathbf{M}_1$  and volume  $V_1$  and shape II with the center in  $\mathbf{M}_2$  and volume  $V_2$  (see Fig. 3). Obviously, the sum of the volumes of the shapes I and II is equal to the original cell volume  $V_1 + V_2 = V_0$ . Then the coefficient  $\bar{d}$  can be evaluated as

$$\bar{d} = \frac{V_1}{V_0} \|\mathbf{M}_1 - \mathbf{M}_F\| + \frac{V_2}{V_0} \|\mathbf{M}_2 - \mathbf{M}_F\| \quad (22)$$

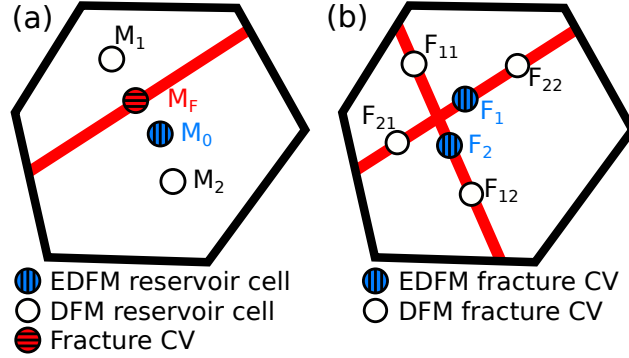


Figure 3: Fluid domain discretization. (a) Control volumes (CV) for EDFM and DFM models. (b) Schematics for fracture-fracture transmissibility calculation.

We next discuss the flux term that arises at the intersection of two fractures. We assume that the flux between two intersecting fracture elements  $F_1$  and  $F_2$  is proportional to the pressure difference (see Fig.3b):

$$Q_{12} = T_2^1 \frac{\rho_f}{\mu} (p_1 - p_2) \quad (23)$$

Hereafter, we denote the transmissibility between two segments  $i$  and  $j$  by  $T_j^i$ . To compute the transmissibility  $T_2^1$  between two intersecting fracture elements  $F_1$  and  $F_2$ , we split these elements by the intersection line into the segments  $F_{11}$ ,  $F_{12}$  and  $F_{21}$ ,  $F_{22}$ , respectively Fig. 3b). Then the transmissibility  $T_2^1$  is obtained with sum of the corresponding transmissibilities:

$$T_2^1 = T_{22}^{11} + T_{21}^{11} + T_{22}^{12} + T_{21}^{12}, \quad (24)$$

where the transmissibilities between the fracture segments (in the right-hand side of Eq. 24) are computed with the star-delta transformation [Karimi-Fard et al., 2003].

## 3.2 Mechanics

### 3.2.1 Stress continuity

We now discuss the discretization of the mechanical system that consists of Eq. 6 and the system (15). Using the enhanced assumed strain approach, we apply finite-element approximations to Eq. 6 [Simo and Rifai, 1990]:

$$\int_{\Omega^e} \nabla^s \boldsymbol{\eta} : \mathbf{S} \, d\Omega = \int_{\Omega^e} \rho \mathbf{g} \, d\Omega, \quad (25a)$$

$$\int_{\Omega^e} \boldsymbol{\gamma} : \mathbf{S} \, d\Omega = 0, \quad (25b)$$

where  $\boldsymbol{\eta}$  denotes a continuous test function,  $\boldsymbol{\gamma}$  is the variation of the enhanced strain, and  $\Omega^e$  is an element that contains a fracture. Eq. 6 transforms into a system of two equations due to singular strain across the fracture. To solve the coupled system (6) and (5), we use the contact integral in Eq. 25b as an additional constraint. This expression must be modified for the case of piecewise constant jump values [Borja, 2000] and can be replaced by the local stress-continuity condition [Regueiro and Borja, 1999, Callari et al., 2010]:

$$\frac{1}{V^e} \int_{\Omega^e} \mathbf{S} \cdot \mathbf{n} \, d\Omega = \mathbf{t} + p_f \mathbf{n} \quad (26)$$

Eq. 26 relates the average total stress  $\bar{\mathbf{S}}$  in an element to the fracture traction  $\mathbf{t}$  and fracture pressure  $p_f$ . Hereafter, we use the following notation  $\overline{(\bullet)} := \frac{1}{V^e} \int_{\Omega^e} (\bullet) \, d\Omega$ . Therefore, in order to complete the system (15), we use the volume average of Eq. 15a

$$\dot{\bar{\boldsymbol{\sigma}}} = \mathbf{C} : \left[ \nabla^s \dot{\mathbf{u}}_c - ([\dot{\mathbf{u}}] \otimes \nabla f)^s \right], \quad (27)$$

and the following relationship between the average effective stress and fracture traction:

$$\mathbf{t} + p_f \mathbf{n} = \bar{\boldsymbol{\sigma}} \cdot \mathbf{n} + b p_M \mathbf{n}. \quad (28)$$

We emphasize that the average effective stress  $\bar{\boldsymbol{\sigma}}$  and jump  $[u]$  are functions of the matrix and fracture pressures and have the corresponding terms in linearization as discussed in Section 3.2.2. Note the absence of the overline above the jump  $[u]$  as  $[u] = [\bar{u}]$  due to the piecewise-constant jump assumption.

In our formulation, we solve the local system of equations (15), (27), and (28) for all the elements containing fractures using the Newton-Raphson method. We use slip rate  $[\dot{\mathbf{u}}]$ , average stress tensor  $\bar{\boldsymbol{\sigma}}$ , and the Lagrange

multiplier  $\lambda$  as primary unknowns. Nodal displacement  $\mathbf{u}_c$ , matrix and fracture pressure  $p_M$  and  $p_F$  are fixed during the nonlinear iterations. In order to obtain quadratic convergence for the system (25), a consistent stress linearization must be performed [Borja, 2013].

### 3.2.2 Stress Linearization

Eq. 27 and Eq. 15b-d constitute a complete system, which is used to find the jump  $[\mathbf{u}]$  and traction vector  $\mathbf{t}$  from the strain  $\boldsymbol{\varepsilon}$ . After computing these quantities, the effective stress  $\boldsymbol{\sigma}$  in Gauss quadrature points can be obtained with Eq. 15a. The effective-stress derivatives can be computed from the following linearization:

$$d\boldsymbol{\sigma} = \mathbf{C} : \left[ \mathbf{I} + \left( \frac{\partial[\mathbf{u}]}{\partial\boldsymbol{\varepsilon}} \otimes \nabla f \right)^s \right] d\boldsymbol{\varepsilon} + \mathbf{C} : \left( \frac{\partial[\mathbf{u}]}{\partial p_f} \otimes \nabla f \right)^s dp_f + \mathbf{C} : \left( \frac{\partial[\mathbf{u}]}{\partial p_m} \otimes \nabla f \right)^s dp_m. \quad (29)$$

The derivatives  $\frac{\partial[\mathbf{u}]}{\partial p_f}$  and  $\frac{\partial[\mathbf{u}]}{\partial p_m}$  can be obtained from the system (15). To evaluate these derivatives and obtain quadratic convergence of the Newton scheme, we use an approach based on the inverse theorem and automatic differentiation as discussed elsewhere [Garipov et al., 2018]. Using Eq. 7, we write the linearization for the total stress tensor:

$$d\mathbf{S} = \mathbf{C} : \left[ \mathbf{I} + \left( \frac{\partial[\mathbf{u}]}{\partial\boldsymbol{\varepsilon}} \otimes \nabla f \right)^s \right] d\boldsymbol{\varepsilon} + \mathbf{C} : \left( \frac{\partial[\mathbf{u}]}{\partial p_f} \otimes \nabla f \right)^s dp_f + \mathbf{C} : \left[ \left( \frac{\partial[\mathbf{u}]}{\partial p_m} \otimes \nabla f \right)^s + b\mathbf{I} \right] dp_m \quad (30)$$

We emphasize that the linearization of the total stress with respect to the matrix pressure  $p_m$  is not isotropic due to the term  $\left( \frac{\partial[\mathbf{u}]}{\partial p_m} \otimes \nabla f \right)^s$ .

## 4 Results

In this section we validate presented mechanical model with plane-strain analytical solutions and compare its spatial convergence with that of the DFM model. The simulation cases presented in this section are computed in a domain with a single cell in the third (z) direction since the available analytical solutions are derived based on the plain-strain assumption. The domain size was assumed ten times larger than the fracture length to mimic an infinite plane. Further we use the term EDFM (embedded discrete fracture model) to refer to both the mechanical and flow models. In the context of mechanics, the terms EDFM and SDA are interchangeable.

## 4.1 Mechanical tests

First, we consider an inclined fracture slipping under compressive loading conditions. Here, a single fracture with length  $l = 10$  m and striking at  $\alpha = 30^\circ$  is slipping due to the applied compressive load  $\sigma_x = 10$  MPa ( $\sigma_y = 0$ ). The tangential slip on the fracture has a parabolic profile [Phan et al., 2003]:

$$[u_\tau] = \frac{4(1-\nu^2)}{E} \sigma_x \sin \alpha (\cos \alpha - \mu \sin \alpha) \sqrt{l^2 - (x-l)^2} \quad (31)$$

where  $E$  is the rock Young's modulus and  $\nu$  is the rock Poisson's ratio.

Second, we consider an open fracture test. In this case, an  $x$ -aligned fracture ( $\alpha = 0$ ) opens due to the applied tensile load  $\sigma_y = 10$  MPa ( $\sigma_x = 0$ ). This problem is analogous to the well-know Sneddon's problem of a pressurized fracture in a plane-strain infinite domain [Sneddon and Elliot, 1946]. The analytical solution for the fracture aperture as a function of the  $x$ -coordinate is given by:

$$[u_n] = \frac{1-\nu}{\mu} \sigma_y \sqrt{l^2 - (x-l)^2} \quad (32)$$

where  $\mu$  is the rock shear modulus. All the geometrical and mechanical parameters used in the simulations are listed in Table 1.

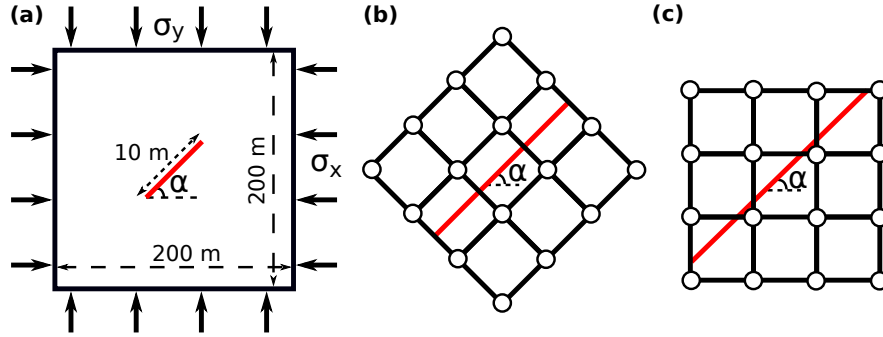


Figure 4: (a) Simulation domain. (b) A fracture conforming to the grid. (c) A fracture not conforming to the grid.

Property	Value
Domain size [m <sup>3</sup> ]	200 × 200 × 10
Fracture length [m]	10
Matrix Young's modulus $E$ [MPa]	10 <sup>3</sup>
Matrix Poisson's ratio $\nu$ [-]	0.25
Friction coefficient $\mu$ [-]	0.6
Dilation coefficient $\theta$ [-]	0.0
Initial cohesive strength $q_0$ [MPa]	0.0
Hardening parameter $H$ [MPa]	0.0

Table 1: Geometrical and material parameters used in the mechanical simulations.

#### 4.1.1 Grid conforming to the fracture

We first present modeling results obtained on a domain with the grid conforming to the fracture (Fig. 4b). We performed several simulations on hexahedral grids with various numbers of cell elements containing the fracture  $n_F = 4, 8, 16,$  and  $32$ . Identical cases with the same grid element sizes were simulated with the DFM model. The tangential jump on the fracture surfaces given by EDFM and DFM models at various grid refinement levels, as well as the analytical solution, are shown in Fig. 5a-b. All slip values are normalized by the maximum of Eq. 31. The coordinates are normalized by the fracture length  $l$ . The solution obtained from the EDFM model overestimates the jump value and converges monotonically to the analytical solution (Fig. 5a). In contrast, the solution obtained from the DFM model underestimates the jump and also converges monotonically to the analytical solution (Fig. 5b).

The  $L_2$ -error in the solutions produced by the EDFM and DFM models as functions of the grid element size is shown in Fig. 5b. Both errors given by DFM and EDFM models reduce while refining the grid at approximately the same rate. In the same figure, we provided linear and quadratic trends to illustrate the order of spatial convergence of the models. The errors given by DFM and EDFM models exhibit super-linear convergence.

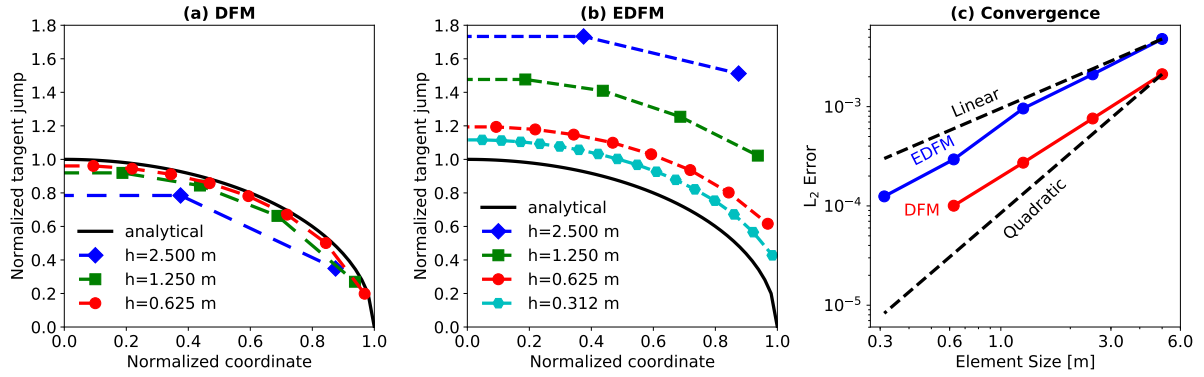


Figure 5: Spatial convergence exhibited by the EDFM and DFM models for the shear problem. (a) Tangential jump as a function of coordinate obtained at various refinement levels. Note that DFM model underestimates the jump, whereas EDFM overestimates it. (b)  $L_2$ -error in the tangential jump value as a function of the element size  $h$ . Both models manifest super-linear convergence. The error in the tangential jump obtained with the DFM model is lower than that obtained with the EDFM model.

For the second test problem, we also performed a convergence analysis of the DFM and EDFM models on Cartesian grids with the numbers of grid comprising the fracture  $n_F = 2, 4, 8, 16,$  and  $32$ . The fracture aperture given by the EDFM and DFM models at various grid refinement levels, as well as the analytical solution, are shown in Fig. 6a-b. Both models underestimate the aperture value and converge monotonically to the analytical solution.

The  $L_2$ -errors in fracture aperture as functions of the grid element size are shown in Fig. 6c. Same as in the previous case, the results obtained from the DFM model manifest super-linear convergence. In contrast, the EDFM convergence in this case is different: at coarse grids the  $L_2$  error  $e$  as a function of the element size  $h$  has the slope less steep than the linear trend; at fine grids the slope of the convergence curve is super-linear ( $e \propto h^{1.24}$ ). Another notable difference with the case of a sliding fracture is that the numerical error given by the EDFM model at coarse grids (less than eight elements per fracture) is less than that of the DFM model. At fine grids (more than eight elements per fracture) the DFM model predicts the fracture aperture more accurately than the EDFM model.

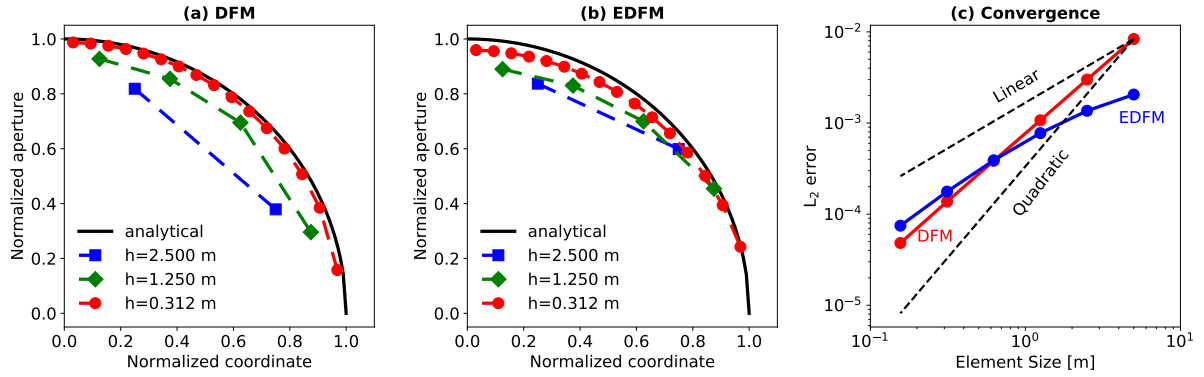


Figure 6: Spatial convergence manifested by the EDFM and DFM models for the opening problem. (a-b) Fracture aperture as a function of the coordinate obtained with the DFM (a) and EDFM (b) models. (c)  $L_2$ -error in the fracture aperture as a function of the grid element size. DFM model manifests super-linear convergence. EDFM model exhibits convergence that is worse than linear trend on coarse grids and linear convergence on fine grids.

#### 4.1.2 Grid not conforming to the fracture

In this section, we present EDFM simulation results for the cases of slipping and opening fractures with the problem setup identical to that in Section 4.1.1. The only difference with the previously-presented simulations is the grid, which does not conform to the fracture (see Fig. 4c).

For the case of a slipping fracture we performed numerical simulations on Cartesian grids with the element sizes  $h = 2, 1.25, \text{ and } 0.625$  m. In these simulations, we also varied the fracture strike angle  $\alpha = 5^\circ, 10^\circ, 20^\circ, 30^\circ, \text{ and } 40^\circ$  in order to eliminate the effect of fracture orientation. The spatial convergence of the EDFM model for the case of a slipping fracture on non-conforming mesh is summarized in Fig. 7. Fig. 7a-e show the slip along the fracture normalized by the maximum slip given by Eq. 31 as a function of a normalized coordinate along the fracture for particular fracture orientations. Fig. 7a-e indicate that the fracture slip given by EDFM on fine grids ( $h = 0.625$  m) is closer to the analytical solution than that obtained on the coarse grids ( $h = 2.5$  m) for each fracture strike  $\alpha$ . Fig. 7f shows the  $L_2$ -error in the numerical solution as a function of the grid element size at various fracture strike angles. The error in the numerical solution decreases monotonically while refining the mesh for each fracture orientation. The average polynomial fit of the data in Fig. 7f yields  $e \propto h^{1.49}$ , which indicates super-linear convergence.



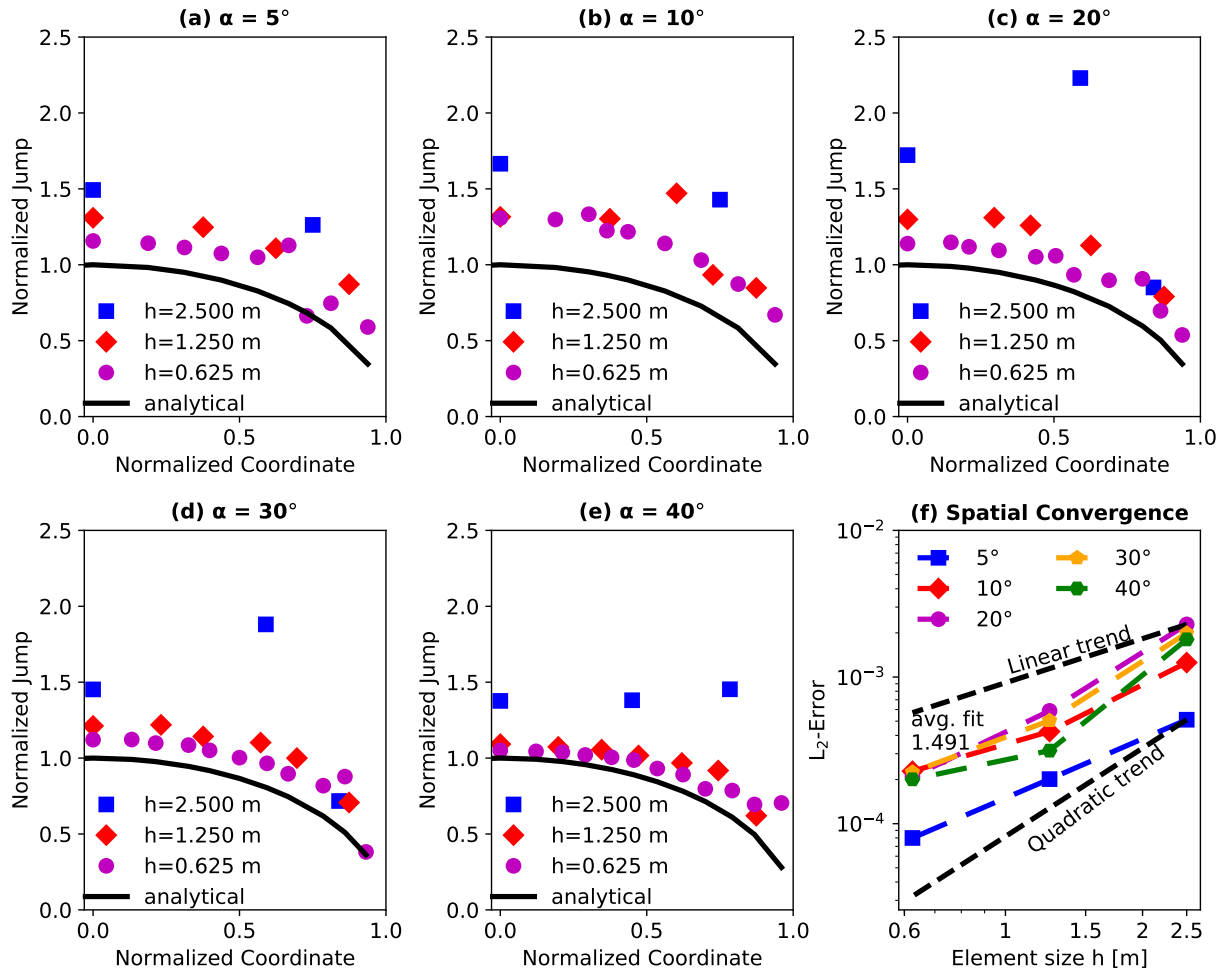


Figure 7: Spatial convergence of the EDFM mode on non-conforming mesh for the fracture slip problem. (a-e) Normalized fracture slip as a function of normalized distance along fracture at various refinement level for various fracture strike angles  $\alpha$ . (f)  $L_2$ -error in tangential jump as a function of mesh element size for various fracture strike angles  $\alpha$ .

We now present the results of a convergence study for the case of an opening fracture on non-conforming grids. Fig. 8a-e show the normalized fracture aperture as a function of the normalized coordinate for various grid element sizes and orientations. Similarly to the case of a slipping fracture, the EDFM model captures poorly the shape of the aperture profile on coarse grids (approximately 3-5 elements per fracture). Upon grid refinement, however, the numerical results converge to the analytical solution for each case of grid orientation.

The spatial convergence of the EDFM model on non-conforming grids for the Sneddon's problem is shown in Fig. 8f. The spatial convergence is monotonic, nonlinear, and differs for various orientation cases. On average, however, the error decreases super-linearly with a decrease in the mesh element size as estimated from the polynomial fit of the data in Fig. 8f  $e \propto h^{1.51}$ .

Overall, the proposed EDFM mechanical model is accurate and converges to the analytical solution. We observe super-linear convergence behavior in all simulation cases on both conforming and non-conforming grids. The DFM model also converges super-linearly and is more accurate than the EDFM model on conforming grids.

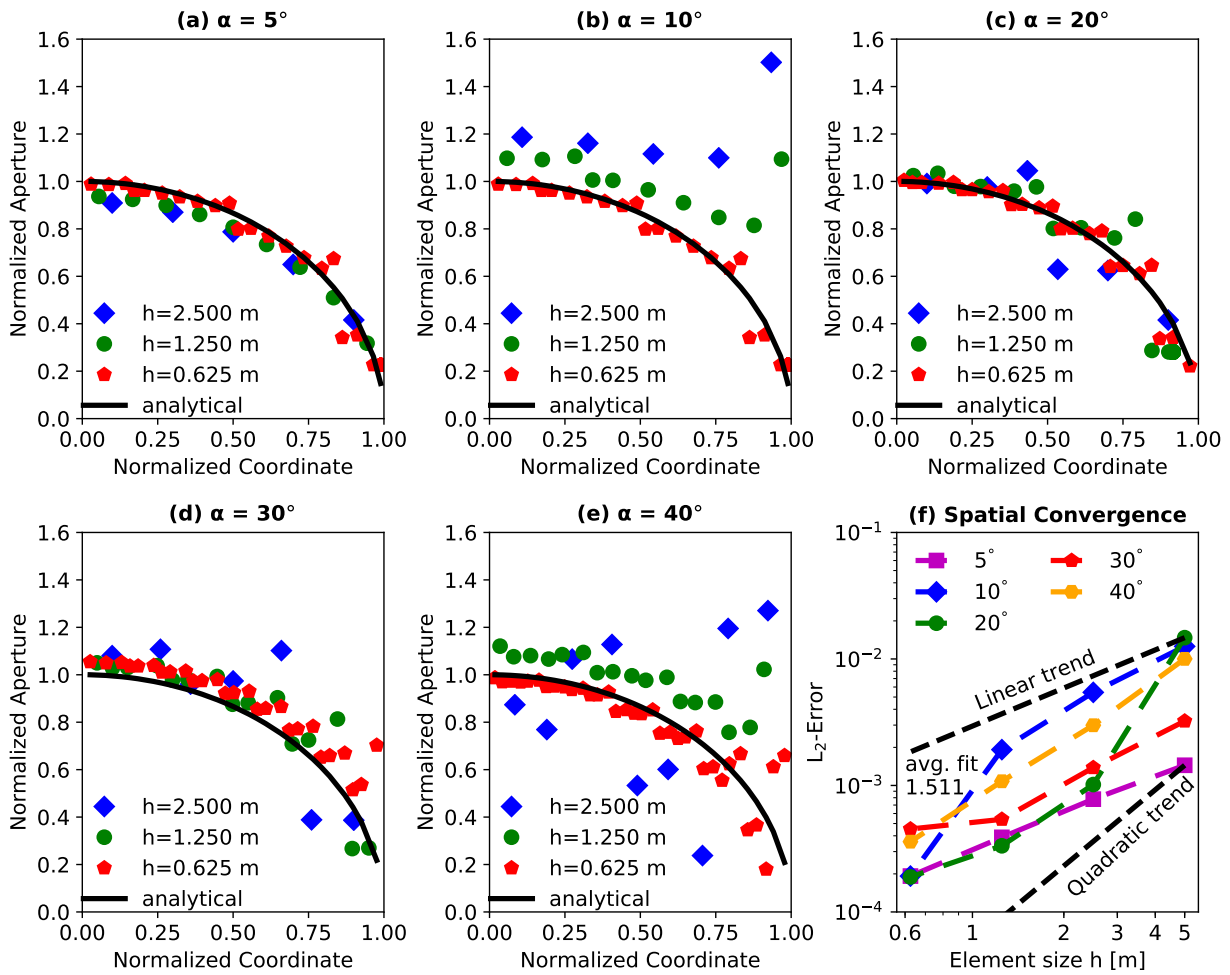


Figure 8: Spatial convergence of the EDFM mode on non-conforming mesh for the fracture opening problem. (a) Normalized fracture aperture as a function of normalized distance along fracture. (b)  $L_2$ -error in fracture aperture as a function of mesh element size.

## 4.2 Fluid flow test

In this section, we validate the proposed approach for the flow problem. The 2D-domain geometry is the same as in the previous tests ( $200 \times 200 \times 10 \text{ m}^3$ ). A single fracture striking at  $140^\circ$  to the x-axis is located in the domain center. The flow parameters of the problem are listed in Table 2. Four wellbores are placed in the corners of the domain as shown in Fig. 9. The wellbore in the left upper corner of the domain is injecting fluid at constant bottom-hole pressure 15 MPa. The rest three wells are production wells with fixed bottom-hole pressure 5 MPa. The initial reservoir pressure is 10 MPa. We apply no-flow condition on all boundaries.

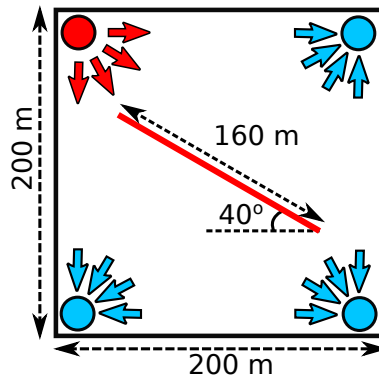


Figure 9: Domain schematics for the flow test problem. The red circle indicates an injection well. The three blue circles indicates production wells. The red straight line shows the fracture.

To validate the EDFM flow model and investigate its spatial convergence, we compare the pressure in the fracture with that obtained with the DFM model on a fine grid ( $h = 0.25 \text{ m}$ ) assumed as the reference solution. We performed four runs of the EDFM model on Cartesian grids with the element sizes:  $h = 4 \text{ m}$ ,  $2 \text{ m}$ ,  $1 \text{ m}$ , and  $0.5 \text{ m}$ . We used the DFM model on a hexahedral unstructured grid with the elements of approximately equal sizes:  $4 \text{ m}$ ,  $2 \text{ m}$ ,  $1 \text{ m}$ ,  $0.5 \text{ m}$ , and  $0.25 \text{ m}$ , the last considered the reference solution.

Property	Value
Domain size [m <sup>3</sup> ]	200 × 200 × 10
Fracture length [m]	160
Fracture strike [°]	140
Fracture conductivity [mD·m]	20
Matrix permeability [mD]	10
Rock porosity [-]	0.2
Initial reservoir pressure [MPa]	10

Table 2: Geometrical and material parameters used in the flow test problem.

The simulation results for the flow test are shown in Fig. 10. Fig. 10a shows the fracture pressure as a function of the coordinate within the fracture at 10, 20, 40 days, and the steady-state solution. The fracture pressure is normalized by the initial reservoir pressure, and the coordinate is normalized by the fracture length  $l$ . The pressure in the fracture decreases with time due to the higher number of producing wells than injection wells. The results in Fig. 10a were obtained from the DFM and EDFM models on the grids with the characteristic element size  $h = 1.0$  m. The DFM and EDFM models provide relatively similar results at this refinement level.

Fig. 10b-c show the steady-state fracture pressure profiles obtained at various refinement levels. Evidently, both DFM and EDFM models overestimate fracture pressure closer to the injector and underestimate it closer towards the producer on coarse grids.

Fig. 10d presents the spatial convergence of the results given by DFM and EDFM models in the fluid test. As evident from the figure, the EDFM and DFM models manifest very similar convergence behavior with approximately the same slope. We again point out that the results obtained from the DFM model, which may explain a slightly lower error yielded by the DFM model.

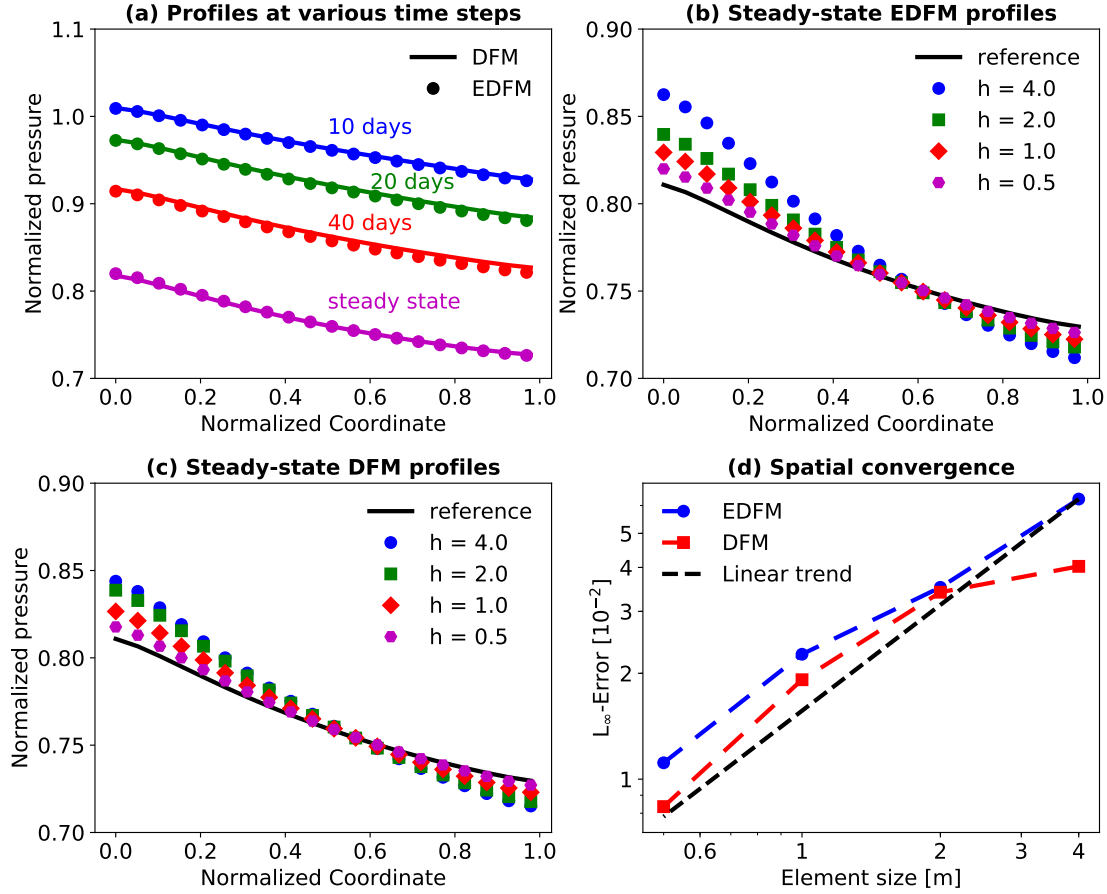


Figure 10: Simulation results for the flow problem. (a) Normalized fracture pressure as a function of coordinate along the fracture at various time instants given by DFM and EDFM models. (b)-(c) Steady-state fracture pressure given by the EDFM (b) and DFM (c) models at various grid resolutions. (d) Spatial convergence of the steady-state solutions: both DFM and EDFM models exhibit linear convergence.

### 4.3 Coupled flow-mechanical test

In this section we present a comparison of the DFM and EDFM models in a coupled 3D case. Fig. 11 shows a reservoir with nine variously-oriented fractures and five wellbores. The domain dimensions are the same as in the previous examples. The initial reservoir pressure is 10 MPa. Four wells located in the four corners of the domain produce fluid with the bottom-hole pressure 10 MPa. Another well at the center of the domain injects fluid with constant rate  $50 \text{ m}^3/\text{day}$  and is connected to the longest fracture. The fracture geometrical properties are listed in Table 3.

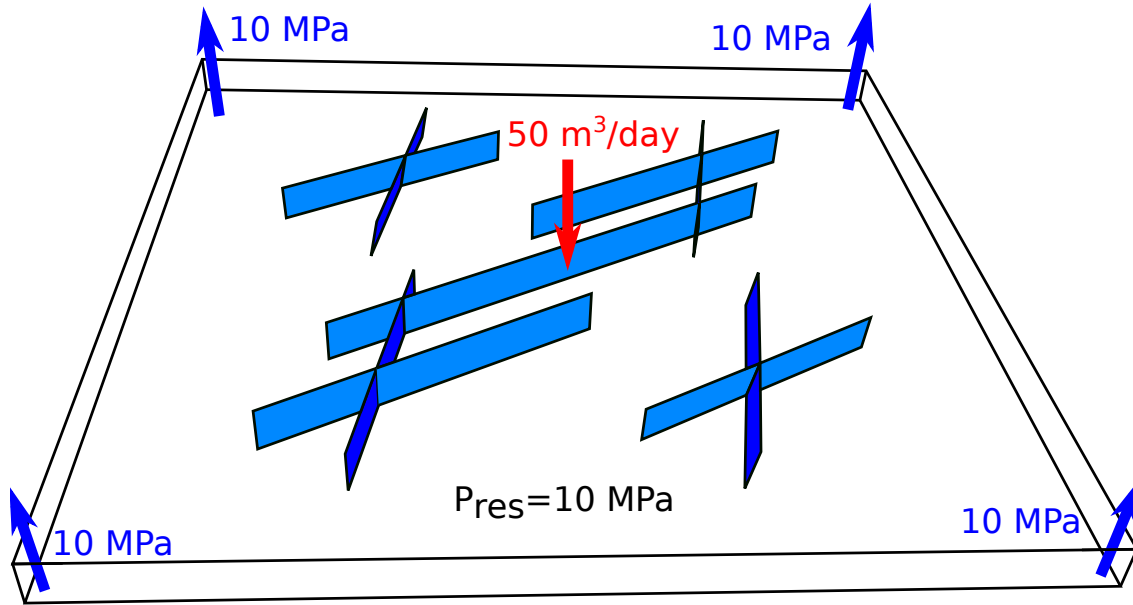


Figure 11: Domain geometry for a coupled problem. The domain comprises nine fractures and five wells. The producing wells are shown in blue. The injection well is connected to the long fracture in the center of the domain and is shown in red.

The reservoir is subjected to anisotropic stresses as follows: the maximum total horizontal stress  $S_{Hmax} = S_x = 30$  MPa, the minimum total horizontal stress  $S_{hmin} = S_y = 24$  MPa, and the total vertical stress  $S_z = 70$  MPa, as shown in Fig. 12. The stress field after the geomechanics initialization procedure (an elastic solution at time = 0) results in various tangent traction  $t$  in different fractures. Fractures #4 and #5 are vertical (have no vertical-stress component) and nearly perpendicular to the maximum horizontal stress  $S_{Hmax}$ . Therefore, they have the lowest initial tangent traction  $t_\tau \approx 10$  MPa. Fractures #1, #2, and #3 are also vertical and strike at  $30^\circ$  to the direction of the maximum horizontal stress  $S_{Hmax}$ , which causes a medium initial tangent traction  $t_\tau \approx 26$  MPa. Fractures #6 and #7 dip at  $80^\circ$ , which results in the initial tangent traction to  $t_\tau \approx 70$  MPa due to the non-zero vertical stress component. Finally, fractures #8 and #9 have the highest tangent traction  $t_\tau \approx 80$  MPa because of the non-vertical orientation (dip =  $80^\circ$ ) and the strike aligned closely to the maximum horizontal stress  $S_{Hmax}$ . All the fractures have constant conductivity 20 mD·m.

We applied the presented DFM and EDFM models to simulate 60 days of injection. The computational domain for the DFM simulation was discretized with an unstructured grid with 59032 tetrahedrons. The grid is fine at the fracture faces (2.2 m) and coarse at the outer domain boundaries (10 m). The mesh has four

cells in the vertical direction near the fractures. The EDFM simulations utilized a Cartesian grid with 40804 hexahedrons. The element size in the horizontal plane is 2 m. Same as the DFM grid, the EDFM grid has four cells in the vertical (z) direction.

Fracture #	Length [m]	Strike [°]	Dip [°]
1	120	30	90
2 and 3	80	30	90
4 and 5	60	80	90
6 and 7	60	80	80
8 and 9	60	30	80

Table 3: Fracture geometrical parameters used in the coupled problem.

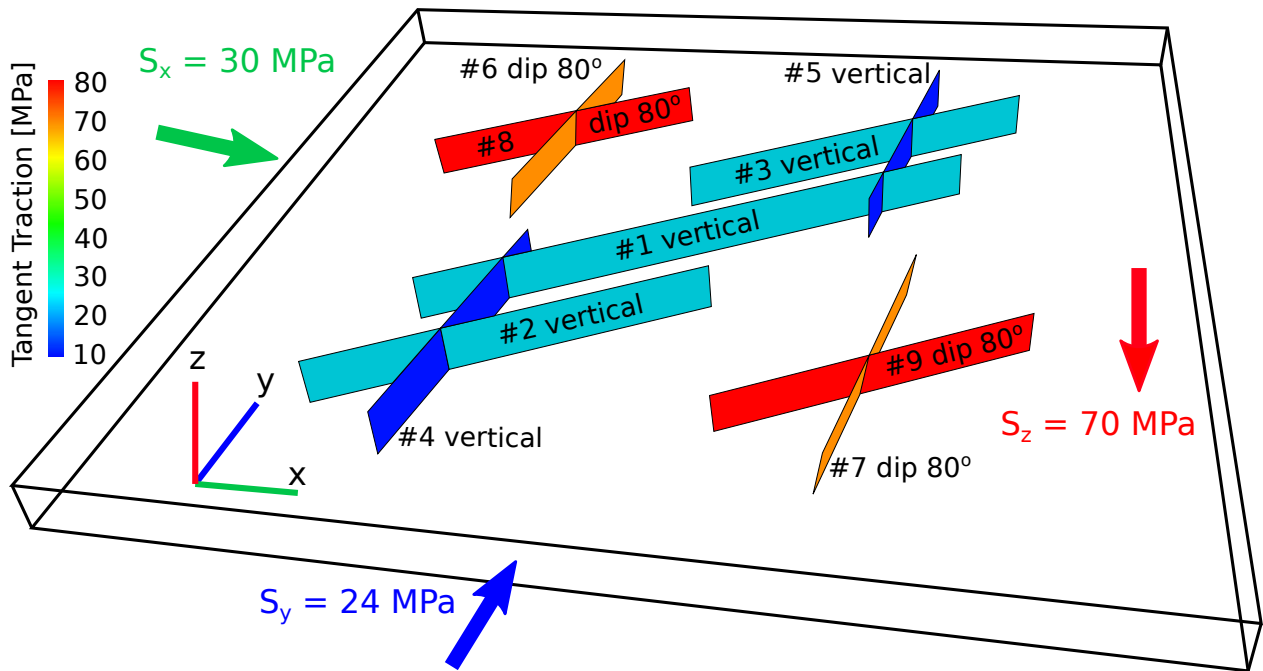


Figure 12: Initial stresses and tangential tractions on fracture surfaces. Vertical fractures #4 and #5 have the lowest initial tangential traction  $t_t \approx 10$  MPa. Vertical fractures #1, #2, and #3 have a medium initial tangential traction  $t_t \approx 25$  MPa. Fractures #6 and #7 dip at  $80^\circ$  and have a high initial tangential traction  $t_t \approx 70$  MPa. Critically-oriented fractures #8 and #9 dip at  $80^\circ$  and have the highest tangential traction  $t_t \approx 80$  MPa.

The process of induced fracture reactivation is illustrated in Fig. 13. At approximately 15 days of injection

the longest Fracture #1 is activated in the center (not shown in Figure). At 27 days of injection about 20% of the area of Fracture #1 is in shear (Fig. 13)a. The activated area is expanding laterally in two directions. The DFM model predicts a higher area of the activated region in Fracture #1 at 27 days. At 31 days of injection, a larger portion ( $\approx 30\%$  area) of Fracture #1 is activated (Fig. 12b). At the same time instant, approximately 40 % area of Fracture #9 is slipping. The activation of Fracture #9 commenced at approximately 19 days (not shown in Figure 12). At 33 days Fracture #8 starts to slip (Fig. 13c). The activated region in Fracture #9 continues to expand laterally towards the inactive end of the fracture. In Fracture #1, the activated region continues to grow bidirectionally.

At 34 days, the opposite end of Fracture #8 is activated in shear so that two slipping regions within the fracture are expanding towards each other 14a. Following the activation of the fractures in shear, tensile activation of Fracture #1 occurred. After 60 days of injection, a small portion of Fracture #1 is open (Fig. 13b). Note that Fractures #2-#7 remained inactive during the injection period. As shown in Fig. 13 and Fig. 14, the DFM and EDFM models yield qualitatively very similar behavior of fracture activation in this complex scenario.



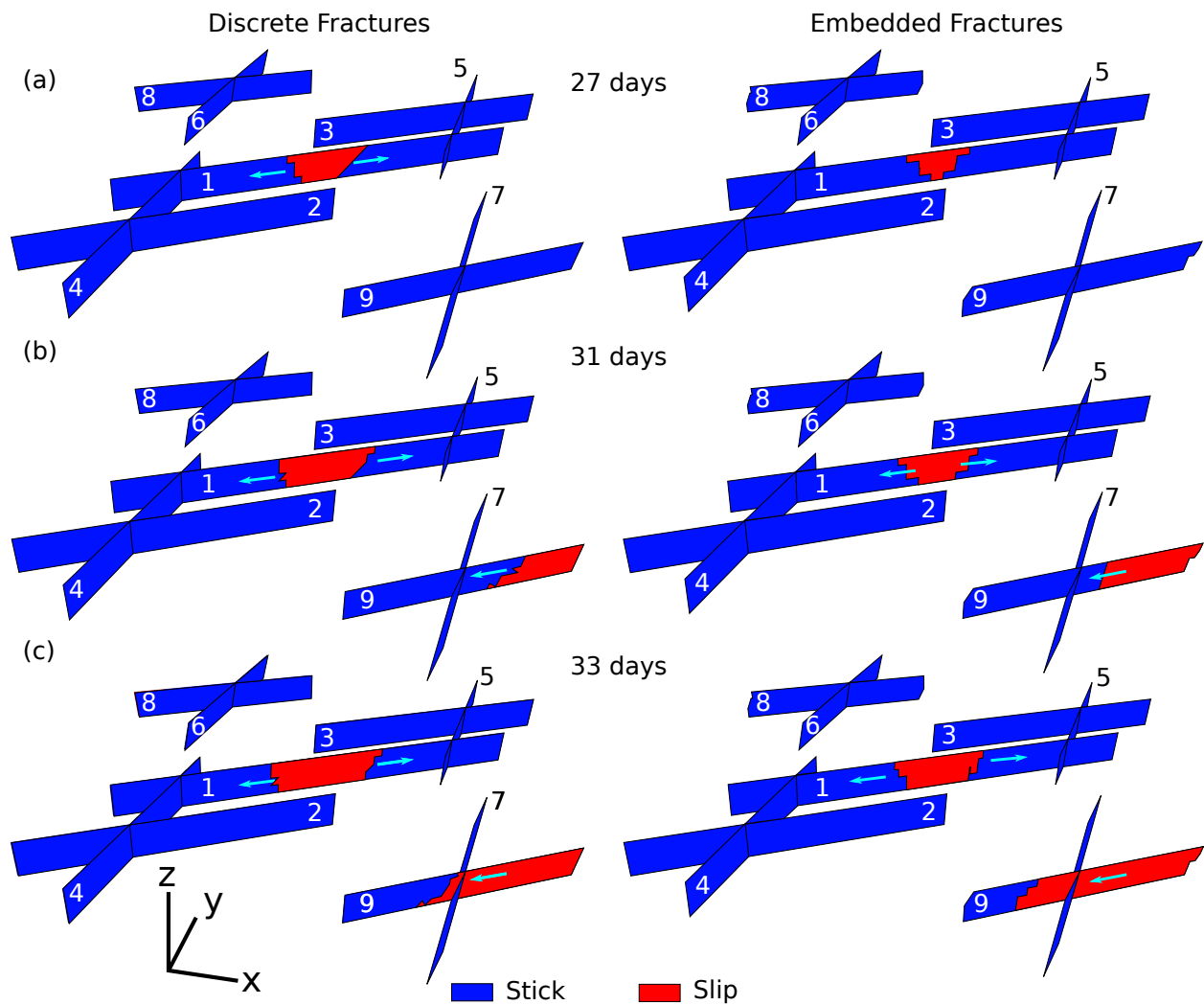


Figure 13: Development of the fracture states predicted by the DFM (left column) and EDFM (right column) methods. The figure shows which fracture elements are inactive (stick) or are active and exhibit slip or opening at various time steps. (a) At 27 days of injection the longest fracture #1 (connected to the injector) is slipping with about 20% of the area activated. The slipping region grows laterally in two directions from the fracture center. (b) At 31 days about 40% of the critically-oriented fracture #9 is slipping. The fracture activated at the farthest point in x direction, and the active region extends laterally. (c) After 33 days 5-15 % of fracture #8 is activated starting from the point with the lowest x-coordinate. Fracture #9 is activated throughout 60-80 % of its area. The activated area in the fracture #1 is approximately the same as at 31 days.

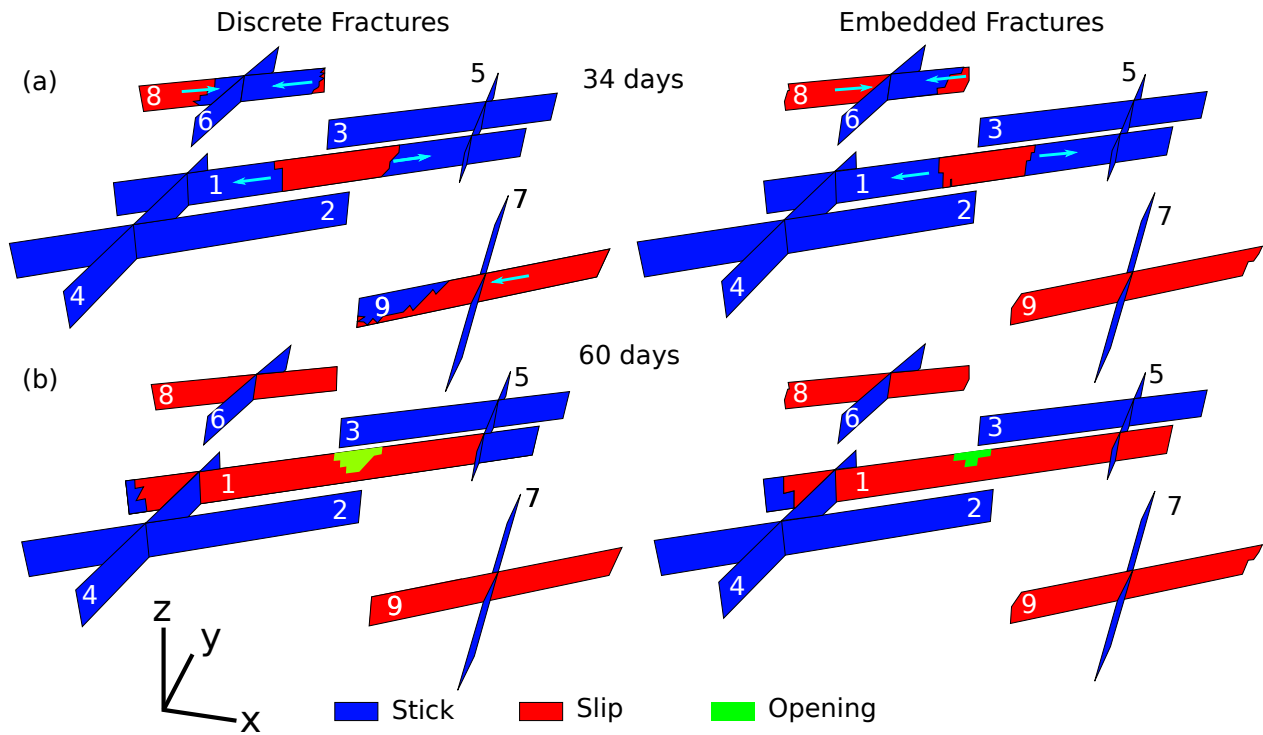


Figure 14: Development of the fracture states predicted by the DFM (left column) and EDFM (right column) methods. (a) Fracture #8 is also activated on the another end at 34 days. From 50 to 70 % of the area of fracture #8 is slipping. (b) Fracture #1 exhibits opening in the center at 60 days.

We now compare the fracture slip values predicted by the DFM and EDFM models within the fractures #1, #2, and #3 at various time steps (Fig. 15). The jump values shown in Fig. 15 are obtained along straight lines at the vertical centers of the fractures. Fig. 15a shows the slip values of the longest Fracture #1 at 27, 34, and 40 days of injection as functions of the coordinate along the fracture. The maximum slip across the fracture increases with time. As evident from Fig. 13, the active region within the fracture expands, and, therefore, the tangential jump within the fracture is localized within a larger region at late times than than at early times. The DFM and EDFM models yield similar values of the slip and similar activated areas for Fracture #1.

Fig. 15b shows the tangential jump values within Fracture #9 at 34 and 40 days. We are not showing the curve for 27 days since the fracture was completely inactive at that time instant. The fracture activated on the right (coordinate  $\approx 60$ ), and the activated region expanded to the left. According to the EDFM mode, at 34 days the fracture was completely activated (Fig. 14), whereas the DFM model yields only approximately

three quarters of the fracture activated. The DFM model also predicts a lower slip value than the EDFM model. At 40 days, Fracture #9 is fully-activated according to both DFM and EDFM models.

Fig. 15c shows the slip values in Fracture #8 at 34 and 40 days. Similarly to Fracture #9, the EDFM model predicts a larger activated area in Fracture #8 at 34 days than that predicted by the DFM model. At 40 days both models predict the full activation of the fracture. The EDFM model predicts higher slip values than the DFM model at both 34 and 40 days.

The activation of Fractures #8 and #9 is due to the increased fluid pressure that reduces the fracture normal traction and drives the fracture to slip. At the same time, the fact that Fracture #9 activated before Fracture #8 is due to the asymmetry of the mechanical problem: we fixed the corresponding displacement components at the bottom, left, and front boundaries, and assigned normal tractions on the opposing boundaries.

All in all, the presented hydro-mechanical simulations evidence the complexity of the fracture behavior during fluid injection. Our DFM and EDFM models provide qualitatively similar results and yield similar dynamics of the fracture activation. The difference in the tangential jump given by the DFM and EDFM models are due to slight differences in fluid pressure and because the EDFM model overestimates fracture slip, whereas the DFM model underestimates it as exemplified in previous sections.

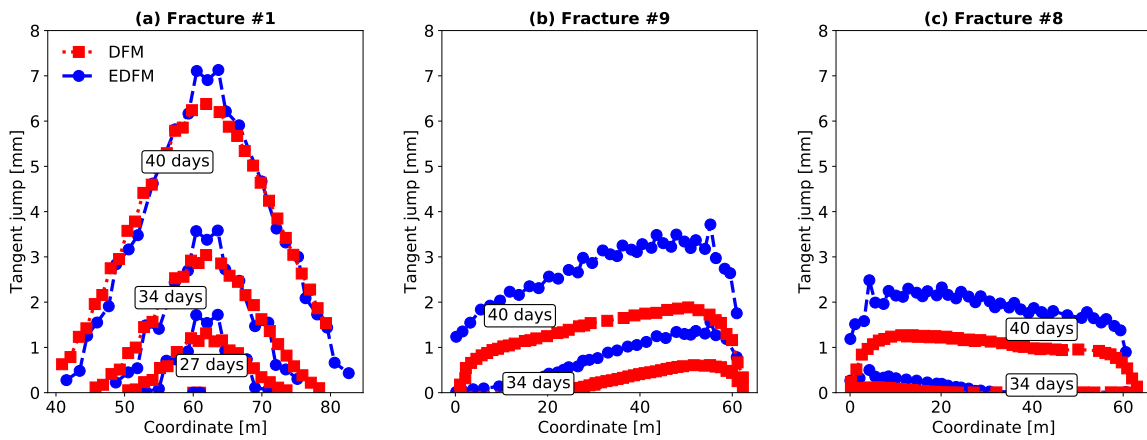


Figure 15: Fracture slip values as a functions of the coordinate at various time steps in (a) Fracture #1. (b) Fracture #9. (c) Fracture #8.

## 5 Discussion

This section evaluates the performance of the proposed EDFM model and discusses its limitations. We also provide an insight into the modeling cases where using EDFM or DFM is more preferable.

### 5.1 Limitations of the model

All the examples with slipping fractures shown in Section 4 indicate that EDFM overestimates the slip. Moreover, the results evidence that the tangential jumps given by EDFM are always higher than those computed with the DFM model. This is presumably due to the locking effect in the proximity of the fracture tip caused by the continuous slip interpolation in the DFM model [Borja, 2013]. The near-tip solution can potentially be improved by assuming non-constant jump within an element [Linder and Armero, 2007]. Additionally, using EDFM on non-conforming grids results in non-smooth displacement profiles, which, in turn, may cause non-physical stress and traction values in active fractures. This trait of the numerical model may be undesirable in stress-sensitive reservoirs, especially if fracture permeability is computed as a function of stress [Rutqvist, 2015, Shovkun and Espinoza, 2017]. In addition, this also may cause convergence issues in fully-coupled models. Therefore, we suggest to use the DFM approach in cases when a smooth jump is required.

The issue with non-realistic stresses in the SDA models can be circumvented by enforcing the continuity of the jump [Deb and Jenny, 2017]. Requiring it, however, results in a non-locality in the numerical treatment of the jump. An alternative way to circumvent the deficiencies associated with computing the mechanics-dependent fracture permeability with the presented SDA model is to assign permeability as a function of fracture aperture [Zimmerman et al., 1991, Shovkun and Espinoza, 2019]. Since fracture aperture is widely used to calculate the permeability of open-mode fractures with the lubrication theory [Lee et al., 2017, Shovkun and Espinoza, 2019] and given the capability to handle arbitrary fracture geometries, SDA is potentially suitable for modeling open-mode fracture propagation. A hybrid formulation that makes use of both SDA and DFM methods for various types of fractures can potentially be an optimal approach for coupled hydro-mechanical modelling of fractured reservoirs.

## 5.2 SDA formulation for intersecting fractures

In this section we outline the basic idea behind the mechanical treatment of fracture intersection in our SDA model. When more than one embedded fracture are located in a grid element, the contact mechanics is described with the following system:

$$\dot{\boldsymbol{\sigma}} = \mathbf{C} : \left[ \nabla^s \mathbf{u}_c - \sum_{i=1}^{N_F} ([\dot{\mathbf{u}}]_i \otimes \nabla f_i)^s \right] \quad (33a)$$

$$[\dot{\mathbf{u}}]_i = \lambda_{\delta_i} \frac{\partial G_i}{\partial \mathbf{t}_i}, \quad i = 1 \dots N_F \quad (33b)$$

$$\dot{q}_i = -\lambda_{\delta_i} H_{\delta_i} \frac{\partial G_i}{\partial q_i}, \quad i = 1 \dots N_F \quad (33c)$$

$$\lambda_{\delta_i} F_i(\mathbf{t}_i, q_i) = 0, \quad i = 1 \dots N_F \quad (33d)$$

where  $N_F$  is the number of embedded fractures in the cell,  $[\mathbf{u}]_i$  are the fracture jump vectors,  $\lambda_i$  are fracture plastic multipliers,  $q_i$  are the fracture internal state variables,  $H_{\delta_i}$  are the fracture hardening moduli,  $\mathbf{t}_i$  is the fracture traction, and  $F_i$  and  $G_i$  are the flow rules plastic potentials, respectively. The system (33) is the direct analogue to (15). All other equations and the solution procedure remain the same as in the case of a single fracture. Therefore, adding a fracture to the system consists of (1) imposing independent constraints (33)b-c on variables related to a particular fracture and (2) using the superposition of jumps to determine the stress (Eq. 33a). Thus, coupling several EDFM fractures within a cell occurs via the effective stress  $\boldsymbol{\sigma}$ .

This strategy has two drawbacks. First, formulation (33) permits the maximum of two embedded fractures per grid element. Applying this approach to more than two fractures per element results in an over-determined system.

Second, each combination of fracture states (e.g. the first fracture is slipping and the second fracture is opening) requires a special treatment. This treatment consists in relaxing the constraints (16)- (20) to avoid the over-determination of the system (33). Future work is needed to develop a robust procedure for treating fracture intersection with various statuses.

## 5.3 Flow modeling

The approach to modeling embedded fractures discussed in Section 3.1, is a simplified way of describing fluid flow. While providing a relatively accurate approximation for single-phase fluids for highly-permeable

fractures, the traditional EDFM approach has two important limitations. First, standard EDFM cannot simulate fractures with permeability lower than that of the rock matrix [Flemisch et al., 2018]. Second, the standard EDFM cannot accurately capture cross-fracture flow, sometimes referred to as fracture sweeping [Karvounis, 2013]. This effect becomes particularly significant when solving transport equations. Two solutions have been suggested to remove these limitations. Karvounis proposed to modify the computation of the matrix-fracture flow  $q_{MF}$  terms based on the direction of the cell fluxes [Karvounis, 2013]. Projection EDFM (pEDFM) is another approach that modifies the number of connections in an approximation pattern [Tene et al., 2017]. The latter approach can be easily implemented in the connection-based flow simulator as a part of the preprocessing stage [Karimi-Fard et al., 2004],

## 6 Conclusion

In this paper we presented a numerical model that uses the Strong Discontinuity Approach (SDA) for geomechanics and the Embedded Fracture (EDFM) approach for fluid flow. This study validates the use of a coupled EDFM model in relatively complex geological settings.

A series of mechanical tests was performed to compare the performance of the Discrete Fracture Model (DFM) and the proposed EDFM model. Both DFM and EDFM manifest asymptotic super-linear convergence on conforming grids when modeling slipping and opening fractures. On non-conforming grids, the EDFM model manifests a range of convergence behaviors depending on the fracture orientation with respect to the computational grids. On average, however, the EDFM model retains the super-linear convergence trend for both opening and slipping fractures.

Numerical simulation evidences discontinuous slip and aperture within EDFM fractures. On very coarse grids, the absence of jump continuity may result in non-physical jump profiles. Based on the simulations we conclude that EDFM overestimates fracture slip, whereas DFM underestimates it.

We presented a simplified EDFM approach to simulate single-phase fluid flow in fractured porous media. The presented model provides accurate results that are very close to those given by the DFM model. We demonstrated that both methods have similar linear convergence behavior.

Finally, we applied the DFM and EDFM methods to simulate a complex 3D coupled hydro-mechanical problem. We considered a fluid injection scenario that resulted in natural fractures activation induced by

excessive pressure and stress alterations.

Our results indicate that EDFM and DFM methods provide qualitatively similar results. Based on multiple numerical tests, we conclude that EDFM can be considered an alternative approach to model highly fractured reservoirs.

## Acknowledgments

We thank the Reservoir Simulation Industrial Affiliates Consortium at Stanford University (SUPRI-B) for funding this research.

## References

- [Alfaiate et al., 2010] Alfaiate, J., Moonen, P., Sluys, L., and Carmeliet, J. (2010). On the use of strong discontinuity formulations for the modeling of preferential moisture uptake in fractured porous media. Computer methods in applied mechanics and engineering, 199(45-48):2828–2839.
- [Borja, 2000] Borja, R. I. (2000). A finite element model for strain localization analysis of strongly discontinuous fields based on standard galerkin approximation. Computer Methods in Applied Mechanics and Engineering, 190(11-12):1529–1549.
- [Borja, 2013] Borja, R. I. (2013). Plasticity, volume 2. Springer.
- [Cacas et al., 1990] Cacas, M.-C., Ledoux, E., Marsily, G. d., Tillie, B., Barbreau, A., Durand, E., Feuga, B., and Peaudecerf, P. (1990). Modeling fracture flow with a stochastic discrete fracture network: calibration and validation: 1. the flow model. Water Resources Research, 26(3):479–489.
- [Callari and Armero, 2002] Callari, C. and Armero, F. (2002). Finite element methods for the analysis of strong discontinuities in coupled poro-plastic media. Computer Methods in Applied Mechanics and Engineering, 191(39-40):4371–4400.
- [Callari et al., 2010] Callari, C., Armero, F., and Abati, A. (2010). Strong discontinuities in partially saturated poroplastic solids. Computer Methods in Applied Mechanics and Engineering, 199(23-24):1513–1535.

- [Cappa and Rutqvist, 2011] Cappa, F. and Rutqvist, J. (2011). Modeling of coupled deformation and permeability evolution during fault reactivation induced by deep underground injection of CO<sub>2</sub>. International Journal of Greenhouse Gas Control, 5(2):336–346.
- [Coussy, 2004] Coussy, O. (2004). Poromechanics. Wiley.
- [Coussy, 2010] Coussy, O. (2010). Mechanics and Physics of Porous Solids. Wiley.
- [Deb and Jenny, 2017] Deb, R. and Jenny, P. (2017). Modeling of shear failure in fractured reservoirs with a porous matrix. Computational Geosciences, 21(5-6):1119–1134.
- [Duarte et al., 2000] Duarte, C. A., Babuška, I., and Oden, J. T. (2000). Generalized finite element methods for three-dimensional structural mechanics problems. Computers & Structures, 77(2):215–232.
- [Elf-Aquitaine, 1992] Elf-Aquitaine, F. (1992). Monitoring of subsidence and induced seismicity in the El-Ael gas field (France): the consequences on gas production and field operation. Engineering Geology, 32:123–135.
- [Flemisch et al., 2018] Flemisch, B., Berre, I., Boon, W., Fumagalli, A., Schwenck, N., Scotti, A., Stefansson, I., and Tatomir, A. (2018). Benchmarks for single-phase flow in fractured porous media. Advances in Water Resources, 111:239–258.
- [Foster et al., 2007] Foster, C., Borja, R., and Regueiro, R. (2007). Embedded strong discontinuity finite elements for fractured geomaterials with variable friction. International Journal for Numerical Methods in Engineering, 72(5):549–581.
- [Fu et al., 2016] Fu, P., Hao, Y., Walsh, S. D. C., and Carrigan, C. R. (2016). Thermal drawdown-induced flow channeling in fractured geothermal reservoirs. Rock Mechanics and Rock Engineering, 49(3):1001–1024.
- [Garipov et al., 2016] Garipov, T., Karimi-Fard, M., and Tchelepi, H. (2016). Discrete fracture model for coupled flow and geomechanics. Computational Geosciences, 20(1):149–160.
- [Garipov et al., 2018] Garipov, T., Tomin, P., Rin, R., Voskov, D., and Tchelepi, H. (2018). Unified thermo-compositional-mechanical framework for reservoir simulation. Computational Geosciences, 22(4):1039–1057.



- [Gong et al., 2008] Gong, B., Karimi-Fard, M., Durlofsky, L. J., et al. (2008). Upscaling discrete fracture characterizations to dual-porosity, dual-permeability models for efficient simulation of flow with strong gravitational effects. SPE Journal, 13(01):58–67.
- [Grasso, 1992] Grasso, J.-R. (1992). Mechanics of seismic instabilities induced by the recovery of hydrocarbons. Pure and Applied Geophysics, 139(3-4):507–534.
- [Haddad and Sepehrnoori, 2015] Haddad, M. and Sepehrnoori, K. (2015). Integration of xfem and czm to model 3d multiple-stage hydraulic fracturing in quasi-brittle shale formations: Solution-dependent propagation direction. In Proceedings of the AADE National Technical Conference and Exhibition, AADE2015, San Antonio, Texas, 8-9 April 2015.
- [Hansbo and Hansbo, 2002] Hansbo, A. and Hansbo, P. (2002). An unfitted finite element method, based on nitsches method, for elliptic interface problems. Computer methods in applied mechanics and engineering, 191(47-48):5537–5552.
- [Heister et al., 2015] Heister, T., Wheeler, M. F., and Wick, T. (2015). A primal-dual active set method and predictor-corrector mesh adaptivity for computing fracture propagation using a phase-field approach. Computer Methods in Applied Mechanics and Engineering, 290:466–495.
- [Hwang et al., 2015] Hwang, J., Bryant, E. C., Sharma, M. M., et al. (2015). Stress reorientation in water-flooded reservoirs. In SPE Reservoir Simulation Symposium. Society of Petroleum Engineers.
- [Karimi-Fard et al., 2004] Karimi-Fard, M., Durlofsky, L., and Aziz, K. (2004). An efficient discrete-fracture model applicable for general-purpose reservoir simulators. SPE Journal, 9(2):227–236.
- [Karimi-Fard et al., 2003] Karimi-Fard, M., Durlofsky, L. J., Aziz, K., et al. (2003). An efficient discrete fracture model applicable for general purpose reservoir simulators. In SPE Reservoir Simulation Symposium. Society of Petroleum Engineers.
- [Karvounis, 2013] Karvounis, D. C. (2013). Simulations of enhanced geothermal systems with an adaptive hierarchical fracture representation. PhD thesis, ETH Zurich.
- [Lee et al., 2017] Lee, S., Wheeler, M. F., and Wick, T. (2017). Iterative coupling of flow, geomechanics and adaptive phase-field fracture including level-set crack width approaches. Journal of Computational and Applied Mathematics, 314:40–60.

- [Li et al., 2015] Li, J., Lei, Z., Qin, G., and Gong, B. (2015). Effective local-global upscaling of fractured reservoirs under discrete fractured discretization. Energies, 8(9):10178–10197.
- [Li et al., 2008] Li, L., Lee, S. H., et al. (2008). Efficient field-scale simulation of black oil in a naturally fractured reservoir through discrete fracture networks and homogenized media. SPE Reservoir Evaluation & Engineering, 11(04):750–758.
- [Linder and Armero, 2007] Linder, C. and Armero, F. (2007). Finite elements with embedded strong discontinuities for the modeling of failure in solids. International Journal for Numerical Methods in Engineering, 72(12):1391–1433.
- [Liu and Borja, 2010] Liu, F. and Borja, R. I. (2010). Stabilized low-order finite elements for frictional contact with the extended finite element method. Computer Methods in Applied Mechanics and Engineering, 199(37-40):2456–2471.
- [McClure, 2012] McClure, M. W. (2012). Modeling and characterization of hydraulic stimulation and induced seismicity in geothermal and shale gas reservoirs. PhD thesis, Stanford University Stanford, California.
- [Min et al., 2004] Min, K.-B., Rutqvist, J., Tsang, C.-F., and Jing, L. (2004). Stress-dependent permeability of fractured rock masses: a numerical study. International Journal of Rock Mechanics and Mining Sciences, 41(7):1191–1210.
- [Mosler, 2005] Mosler, J. (2005). A novel algorithmic framework for the numerical implementation of locally embedded strong discontinuities. Computer Methods in Applied Mechanics and Engineering, 194(45-47):4731–4757.
- [Mosler and Meschke, 2003] Mosler, J. and Meschke, G. (2003). 3d modelling of strong discontinuities in elastoplastic solids: fixed and rotating localization formulations. International Journal for Numerical Methods in Engineering, 57(11):1553–1576.
- [Narasimhan and Pruess, 1988] Narasimhan, T. and Pruess, K. (1988). Minc: An approach for analyzing transport in strongly heterogeneous systems. In Groundwater Flow and Quality Modelling, pages 375–391. Springer.

- [Norbeck et al., 2016] Norbeck, J. H., McClure, M. W., Lo, J. W., and Horne, R. N. (2016). An embedded fracture modeling framework for simulation of hydraulic fracturing and shear stimulation. Computational Geosciences, 20(1):1–18.
- [Oliver, 1996] Oliver, J. (1996). Modelling strong discontinuities in solid mechanics via strain softening constitutive equations. part 1: Fundamentals. International journal for numerical methods in engineering, 39(21):3575–3600.
- [Oliver et al., 1999] Oliver, J., Cervera, M., and Manzoli, O. (1999). Strong discontinuities and continuum plasticity models: the strong discontinuity approach. International journal of plasticity, 15(3):319–351.
- [Oliver et al., 2003] Oliver, J., Huespe, A., and Samaniego, E. (2003). A study on finite elements for capturing strong discontinuities. International journal for numerical methods in engineering, 56(14):2135–2161.
- [Olson, 2008] Olson, J. E. (2008). Multi-fracture propagation modeling: Applications to hydraulic fracturing in shales and tight gas sands. In 42nd US Rock Mechanics Symposium and 2nd US-Canada Rock Mechanics Symposium, ARMA 08-237.
- [Ouchi et al., 2015] Ouchi, H., Katiyar, A., York, J., Foster, J. T., and Sharma, M. M. (2015). A fully coupled porous flow and geomechanics model for fluid driven cracks: a peridynamics approach. Computational Mechanics, 55(3):561–576.
- [Phan et al., 2003] Phan, A.-V., Napier, J., Gray, L., and Kaplan, T. (2003). Symmetric-galerkin bem simulation of fracture with frictional contact. International journal for numerical methods in engineering, 57(6):835–851.
- [Pruess, 1992] Pruess, K. (1992). Brief guide to the minc-method for modeling flow and transport in fractured media. Technical report, Lawrence Berkeley Lab., CA (United States).
- [Regueiro and Borja, 1999] Regueiro, R. A. and Borja, R. I. (1999). A finite element model of localized deformation in frictional materials taking a strong discontinuity approach. Finite Elements in Analysis and Design, 33(4):283–315.
- [Regueiro and Borja, 2001] Regueiro, R. A. and Borja, R. I. (2001). Plane strain finite element analysis of pressure sensitive plasticity with strong discontinuity. International Journal of Solids and Structures, 38(21):3647–3672.

- [Rutledge et al., 2004] Rutledge, J., Phillips, W., and Mayerhofer, M. (2004). Faulting induced by forced fluid injection and fluid flow forced by faulting: An interpretation of hydraulic-fracture microseismicity, carthage cotton valley gas field, texas. Bulletin of the Seismological Society of America, 94(5):1817–1830.
- [Rutqvist, 2015] Rutqvist, J. (2015). Fractured rock stress-permeability relationships from in situ data and effects of temperature and chemical-mechanical couplings. Geofluids, 15(1-2):48–66.
- [Salimzadeh et al., 2018] Salimzadeh, S., Paluszny, A., Nick, H. M., and Zimmerman, R. W. (2018). A three-dimensional coupled thermo-hydro-mechanical model for deformable fractured geothermal systems. Geothermics, 71:212 – 224.
- [Sesetty et al., 2012] Sesetty, V., Ghassemi, A., et al. (2012). Simulation of hydraulic fractures and their interactions with natural fractures. In 46th US Rock Mechanics/Geomechanics Symposium. American Rock Mechanics Association.
- [Shovkun and Espinoza, 2017] Shovkun, I. and Espinoza, D. N. (2017). Coupled fluid flow-geomechanics simulation in stress-sensitive coal and shale reservoirs: Impact of desorption-induced stresses, shear failure, and fines migration. Fuel, 195:260–272.
- [Shovkun and Espinoza, 2018] Shovkun, I. and Espinoza, D. N. (2018). Geomechanical implications of dissolution of mineralized natural fractures in shale formations. Journal of Petroleum Science and Engineering, 160:555–564.
- [Shovkun and Espinoza, 2019] Shovkun, I. and Espinoza, D. N. (2019). Propagation of toughness-dominated fluid-driven fractures in reactive porous media. International Journal of Rock Mechanics and Mining Sciences.
- [Simo and Oliver, 1994] Simo, J. and Oliver, J. (1994). A new approach to the analysis and simulation of strain softening in solids. Fracture and damage in quasibrittle structures, pages 25–39.
- [Simo et al., 1993] Simo, J. C., Oliver, J., and Armero, F. (1993). An analysis of strong discontinuities induced by strain-softening in rate-independent inelastic solids. Computational mechanics, 12(5):277–296.

- [Simo and Rifai, 1990] Simo, J. C. and Rifai, M. (1990). A class of mixed assumed strain methods and the method of incompatible modes. International journal for numerical methods in engineering, 29(8):1595–1638.
- [Sneddon and Elliot, 1946] Sneddon, I. and Elliot, H. (1946). The opening of a griffith crack under internal pressure. Quart. Appl. Math, 4(3):262–267.
- [Sun et al., 2016] Sun, Y., Aman, M., and Espinoza, D. N. (2016). Assessment of mechanical rock alteration caused by co 2–water mixtures using indentation and scratch experiments. International Journal of Greenhouse Gas Control, 45:9–17.
- [Tene et al., 2017] Tene, M., Bosma, S. B., Al Kobaisi, M. S., and Hajibeygi, H. (2017). Projection-based embedded discrete fracture model (pedfm). Advances in Water Resources, 105:205–216.
- [Warren et al., 1963] Warren, J., Root, P. J., et al. (1963). The behavior of naturally fractured reservoirs. Society of Petroleum Engineers Journal, 3(03):245–255.
- [Wiprut and Zoback, 2000] Wiprut, D. and Zoback, M. D. (2000). Fault reactivation and fluid flow along a previously dormant normal fault in the northern north sea. Geology, 28(7):595–598.
- [Zhao et al., 2009] Zhao, X., Young, R., et al. (2009). Numerical simulation of seismicity induced by hydraulic fracturing in naturally fractured reservoirs. In SPE Annual Technical Conference and Exhibition. Society of Petroleum Engineers.
- [Zimmerman et al., 1991] Zimmerman, R., Kumar, S., and Bodvarsson, G. (1991). Lubrication theory analysis of the permeability of rough-walled fractures. In International Journal of Rock Mechanics and Mining Sciences & Geomechanics Abstracts, volume 28, pages 325–331. Elsevier.
- [Zoback, 2013] Zoback, M. D. (2013). Reservoir geomechanics. Cambridge University Press, New York.
- [Zoback and Gorelick, 2012] Zoback, M. D. and Gorelick, S. M. (2012). Earthquake triggering and large-scale geologic storage of carbon dioxide. Proceedings of the National Academy of Sciences, 109(26):10164–10168.
- [Zoback and Zinke, 2002] Zoback, M. D. and Zinke, J. C. (2002). Production-induced normal faulting in the valhall and ekofisk oil fields. In The Mechanism of Induced Seismicity, pages 403–420. Springer.